applied sciences

MDPI

Article

A Comparative Analysis of Active Control vs. Folding Wing Tip Technologies for Gust Load Alleviation

Francesco Toffol

Department of Aerospace Science and Technology, Politecnico di Milano, Via La Masa 34, 20156 Milano, Italy; francesco.toffol@polimi.it

Abstract: As part of the Ultra High Aspect Ratio Wing Advanced Research and Designs (U-HARWARD) project, funded by CS2JU, various gust load alleviation (GLA) technologies have been developed and studied. GLA plays a crucial role in the development of new generation ultra-high aspect ratio wings (UHARWs), as it reduces gust loads, thereby decreasing the structural weight of the wing and, consequently, the entire aircraft. This weight reduction enhances overall aircraft efficiency, enabling a higher aspect ratio. GLA technologies are categorized into passive systems, which require no active intervention, and active systems, where control surfaces redistribute the aerodynamic loads. In this study, passive GLA was implemented using a folding wing tip (FWT) developed by the University of Bristol, while active GLA employed a Static Output Feedback controller developed by Politecnico di Milano. Both approaches were compared against a baseline aircraft configuration. A flutter assessment confirmed that FWT does not introduce aeroelastic instabilities, ensuring the aircraft remains flutter-free across its flight envelope. A thorough comparison of load envelopes, based on nearly 2000 load cases across different flight points and mass configurations, was conducted in compliance with CS25 regulations, examining both positive and negative gust conditions. The results show a possible 15% reduction in the dynamic load envelope for both passive and active solutions. Using NeOPT, a hybrid finite element (FE) model was developed, with a detailed global FEM (GFEM) for the wingbox and stick elements for other components. Linear gust analyses in Nastran, with the hinge locked and released, provided high-fidelity results, comparing wing failure indexes and demonstrating the effectiveness of the FWT solution.

Keywords: high aspect ratio wings; load alleviation; folding wing tip

Citation: Toffol, F. A Comparative Analysis of Active Control vs. Folding Wing Tip Technologies for Gust Load Alleviation. *Appl. Sci.* **2024**, *14*, 9883. https://doi.org/10.3390/app14219883

Academic Editor: Wei Huang

Received: 26 September 2024
Revised: 21 October 2024
Accepted: 23 October 2024
Published: 29 October 2024

1. Introduction

In recent years, research on high aspect ratio wings [1–9] has significantly stimulated the aeroelastic community, leading to extensive work on design challenges, the development of new tools to address increased flexibility, and experimental validation [10]. While the benefits of increasing the aspect ratio, such as reduced induced drag and improved aerodynamic efficiency, are well known, the drawbacks of a more slender wing are considerable. The increased aerodynamic forces, especially the bending moment, demand additional structural mass to withstand the loads, and greater flexibility can introduce aeroelastic instabilities that may compromise aircraft safety (e.g., flutter, control reversal, or divergence). One possible mitigation for reducing the increased load due to the span extension is the use of the folding wing tip (FWT). The concept of folding wings dates back to 1913, when it was first developed and patented by the British manufacturer Short Brothers plc for ship-borne aircraft [11]. By the late 1930s, the folding mechanism had become fully automatic and hydraulic [12], although it remained exclusive to naval aircraft. The first use of a folding wing tip for maneuverability came in the 1960s with [13], where the outer wing could rotate up to 65° to enhance lateral stability at supersonic speeds. Other aircraft have incorporated foldable components to fit within existing airport infrastructure, such as the Saab 37 Viggen's vertical tail. More recently, Boeing introduced the B777X, an upgrade

to the existing B777, featuring folding wing tips that reduce wingspan during ground operations, allowing for a higher aspect ratio without altering the aerodrome reference code [14]. Historically, these designs were primarily aimed at reducing aircraft dimensions when not in flight, either to maximize storage on carriers or to fit within airport spaces. However, the potential for load alleviation through folding wings has been recognized since the late 1930s, when the Rey R.1 prototype was patented [15]. After a long hiatus, McDonnell Douglas revisited the idea in 1999 with a patented folding wingtip featuring load alleviation capabilities. Boeing, in 2004, compared the flared folding wing tip with the aeroelastic tailoring [16], and Airbus UK patented a similar concept in 2007. Since 2013, researchers like Cooper and Wilson have extensively studied this concept, making it a key topic in modern aeroelasticity research. Further information about the history of the folding wing tip concept can be found in [17]. More recently, extensive research and development have been conducted on the design of folding wing tips and the simulation capabilities required to model their behavior [18–25]. In parallel, experimental activities in wind tunnels have also been carried out [10,26–28].

On the other hand, active controllers for gust load alleviation (GLA) have been studied since the 1950s, when a feed-forward controller for GLA enabled a structure to be 20% lighter than required [29]. Since then, various active control techniques have been explored and implemented in both commercial and military aircraft. While a full bibliographic review is beyond the scope of this paper, a comprehensive survey up until 2012 can be found in [30]. Within this context, the U-HARWARD project [2,31,32] explores various technologies to enhance the aspect ratio of aircraft, while minimizing weight increase and addressing aeroelastic phenomena. Specifically, two strategies for gust load alleviation were examined: an active Static Output Feedback (SOF) controller [33,34], which utilizes conventional control surfaces (ailerons and elevators) and developed by Politecnico di Milano, and a flared hinged folding wing tip (FWT) [35–37], investigated by the University of Bristol. In the U-HARWARD project, a dedicated study examined the gust load response of a scaled wind tunnel model equipped with folding wing tips (FWTs) [10]. However, due to budget and time constraints, it was not possible to investigate the active control system.

The aircraft considered in this study is the outcome of previous optimization work [5], in which a baseline medium-range aircraft, similar to an Airbus A321, was modified by increasing the aspect ratio and determining the most efficient configuration. The optimal configuration was found to have an aspect ratio (AR) of 15.

This work compares the pros and cons of two distinct technologies, which have so far been studied separately. More specifically, by using the same model, it becomes possible to quantify the load reduction achieved by both alleviation methods. This provides valuable insights at the conceptual design stage regarding which solution is most effective, the associated system architecture complications, differences in aeroelastic behavior, and the overall impact on aircraft design.

2. Model and Methods

The analysis model used is a standard type commonly employed for dynamic analysis. The structural components are represented using a finite element (FE) stick model, the aerodynamics is handled by a doublet-lattice method (DLM), and non-structural masses (fuel, payload, engines, etc.) are represented by concentrated masses. The model is shown in Figure 1.

Regarding the active controller, the control surfaces already modeled in the aeroelastic model include the ailerons, which move symmetrically, and the elevator. A minor modification to the model was necessary to account for the folding wing tip. Specifically, the outboard section of the wing was modified to incorporate the hinge kinematics. At the location of the hinge, two coincident nodes were introduced, with the two parts connected through a set of multiple point constraints (MPCs), except for the rotational degree of freedom related to the hinge. Additionally, a dedicated coordinate system was added to

replicate the flare angle identified in the study conducted by the University of Bristol [36]. Figure 2 presents a schematic of the model of the flared FWT.

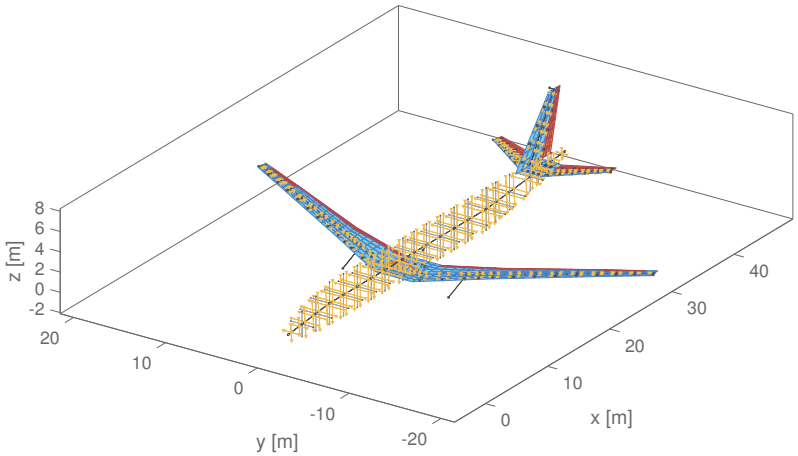

Figure 1. The aeroelastic model of the considered aircraft.

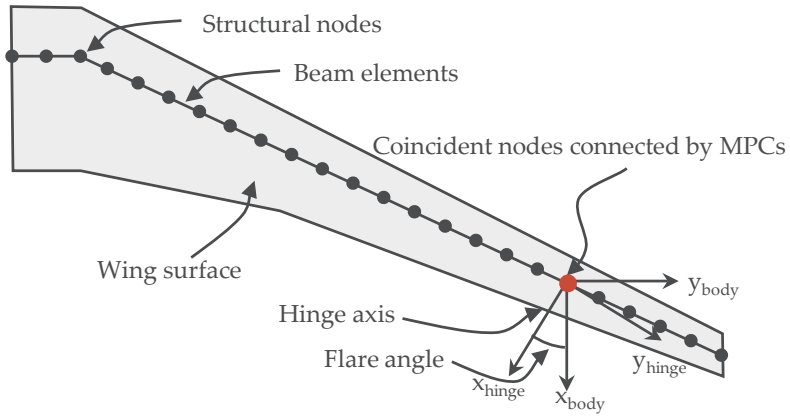

Figure 2. The plan-form view of the wing with the modified kinematics to model the flared FWT.

Although the model is written in Nastran format, the analysis was performed using NeoCASS. NeoCASS includes a feature that identifies the generalized aerodynamic forces (GAFs) using matrix fraction approximation (MFA) [38], which enables the aero-servo-elastic problem to be formulated in the time domain. The aeroelastic problem is expressed in a state-space model, as shown in Equation (1). The subscript x_{ae}, representing the aeroelastic state, indicates that the state vector includes both structural states (modal velocity and displacement) and the aerodynamic states used to determine the unsteady GAFs. The system inputs are the control surface deflections u and the gust v_g. $\mathbf{A}$ is the state or system matrix, $\mathbf{B_\bullet}$ are the inputs matrices, $\mathbf{C}$ is the output matrix and $\mathbf{D_\bullet}$ are the feed-through matrices. A second-order low-pass filter with a cut-off frequency of 15 Hz was applied to mimic the behavior of real actuators.

$$\begin{cases} \dot{\mathbf{x}}_{\mathbf{ae}} & = \mathbf{A}\mathbf{x}_{\mathbf{ae}} + \mathbf{B}_{\mathbf{u}}\mathbf{u} + \mathbf{B}_{\mathbf{g}}\mathbf{v}_{\mathbf{g}} \\ \mathbf{y} & = \mathbf{C}\mathbf{x}_{\mathbf{ae}} + \mathbf{D}_{\mathbf{u}}\mathbf{u} + \mathbf{D}_{\mathbf{g}}\mathbf{v}_{\mathbf{g}} \end{cases} \tag{1}$$

Several flight and mass conditions were analyzed in this work, resulting in the development of multiple state-space models that account for varying aerodynamic conditions (Mach number), as well as different payload and fuel distributions. A constant equivalent air speed (EAS) of $V_{EAS} = 150$ m/s was considered across six different altitudes, ranging from 0 m to 10,000 m in 2000 m increments. The four mass configurations are detailed in Table 1.

Table 1. Mass configurations considered.

Mass Configuration	Payload	Fuel
CONF1	100%	80%
CONF2	80%	100%
CONF3	100%	0%
CONF4	50%	100%

For each flight condition and mass configuration, 20 gusts are considered, with both positive and negative amplitudes. Their 1-cosine gust gradients are evenly spaced between H = 9 m and H = 107 m, in accordance with CS25 regulations [39]. The gust amplitude is calculated using Equation (2), with an alleviation factor of $F_g = 1$. Following the CS 25.341 Gust and Turbulence Loads nomenclature, U_{ds} is the design gust velocity in the equivalent airspeed, U_{ref} is the reference gust velocity in the equivalent airspeed and $\rho_\bullet$ is the air density at sea level (0) and at a prescribed altitude (z).

$$U_{ds} = \sqrt{\frac{\rho_z}{\rho_0}} F_g U_{ref} \left(\frac{H}{107}\right)^{\frac{1}{6}} \tag{2}$$

The gust excitation profile becomes the one in Equation (3)

$$v_g(t) = \frac{U_{ds}}{2}\left(1 - \cos\left(\frac{\pi V_\infty}{H} t\right)\right) \tag{3}$$

The positive gust shapes, for a single flight point with an altitude z = 8000 m are plotted in Figure 3.

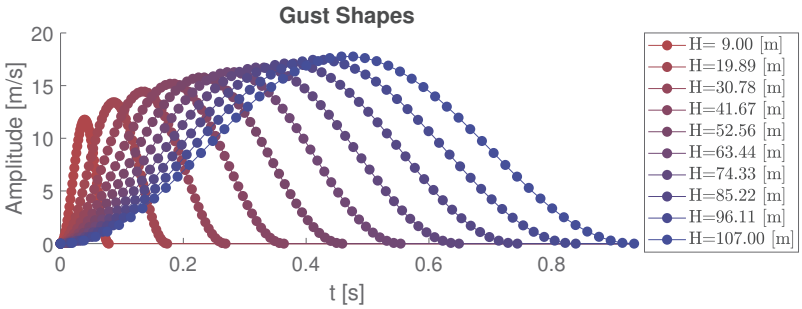

Figure 3. Gust time histories for z = 8000 m and $V_{EAS} = 150$ m/s.

The combination of various gust gradients, mass configurations, altitudes, and worst-case time-correlated loads for bending and torsional moments results in a total of 1920 load conditions that need to be enveloped.

3. Active Control

While FWTs are passive devices that only require proper modeling, the actively controlled GLA requires the synthesis of a controller. In this work, a Static Output Feedback (SOF) controller [40] was designed. This approach was chosen for its simplicity and reliability, as demonstrated in previous numerical and experimental studies [41,42]. The SOF architecture is straightforward: it generates a control input, **u**, which is a linear combination of certain measurements, **y**, as described in Equation (4).

$$\mathbf{u} = -\mathbf{G}\mathbf{y} \tag{4}$$

Aside from time integration, the controller is purely static, meaning there is no filtering of the measured signals or incorporation of controller dynamics. This simplifies the design to determining the gain matrix used to compute the control input, specifically the **G** term in Equation (4). The measurements used for control are the pitch rate, the accelerations at the wing tips, and the center of gravity, which are integrated to obtain the structural

velocity. The control surfaces commanded by the SOF controller are the elevator and the ailerons, which are actuated symmetrically. As the elevator primarily influences the aircraft's rigid body dynamics, its deflection is set to be proportional only to the pitch rate to suppress low-frequency gust content. The resulting gain matrix is structured as shown in Equation (5), with six independent g_i gain values to be defined.

$$\begin{Bmatrix} \delta_{aileron\ RH} \\ \delta_{aileron\ LH} \\ \delta_{elevator} \end{Bmatrix} = - \begin{bmatrix} g_1 & g_2 & g_1 & g_2 & g_3 & g_4 & g_5 \\ g_1 & g_2 & g_1 & g_2 & g_3 & g_4 & g_5 \\ 0 & & & \cdots & & 0 & g_6 \end{bmatrix} \begin{Bmatrix} \ddot{x}_{tip\ RH} \\ \dot{x}_{tip\ RH} \\ \ddot{x}_{tip\ LH} \\ \dot{x}_{tip\ LH} \\ \ddot{x}_{CG} \\ \dot{x}_{CG} \\ q_{CG} \end{Bmatrix} \tag{5}$$

The g_i values were determined using the procedure outlined in [41]. An optimization problem was formulated, with the objective of minimizing the weighted sum of the ratios between the open-loop (OL) and closed-loop (CL) structural responses. Specifically, these ratios were calculated for the bending moments (BMs) and torsional moments (TMs) at the wing root (WR) and engine section (ES), as shown in Equation (6).

$$obj = \frac{WRBM_{CL}}{WRBM_{OL}} + \frac{WRTM_{CL}}{WRTM_{OL}} + \frac{ESBM_{CL}}{ESBM_{OL}} + \frac{ESTM_{CL}}{ESTM_{OL}} \tag{6}$$

The optimization was performed using Matlab's fmincon, ensuring the stability of the closed-loop aero-servo-elastic system across the flight envelope by imposing $\Re(\lambda) < 0$. Additionally, a constraint was applied to limit the control surface rotation rate to $\dot{\delta} \leq 80\frac{^\circ}{s}$.

4. Results for the Stick Model Dynamic Load Computation

This section presents the results for the three different aircraft configurations considered: the baseline aircraft with a cantilevered wing (CNT), the same aircraft equipped with the SOF controller (SOF), and the aircraft with a modified structure to accommodate the flared FWT (FWT). The results, shown in Figure 4, are presented as dynamic load envelopes at the wing root, which is the area subject to the highest loads.

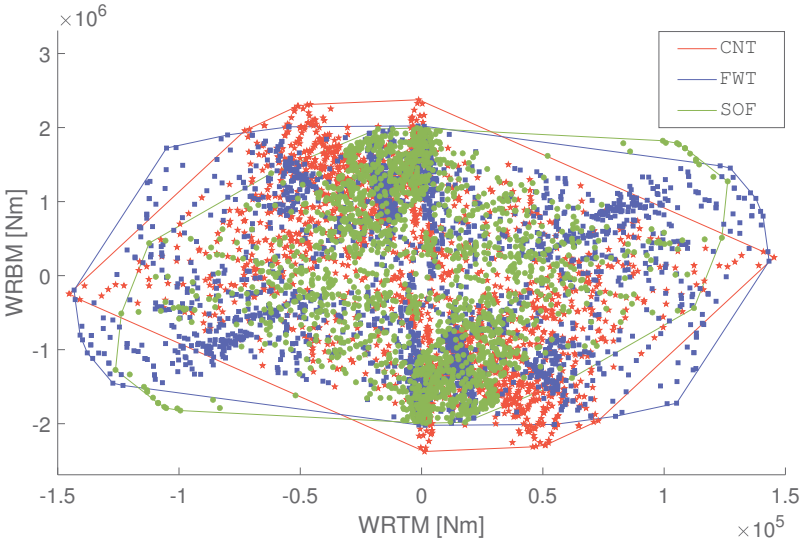

Figure 4. Bending and torsional moment envelope at the wing root for the three models.

Compared with the baseline aircraft, both the active controller and the folding wing tip reduce the dynamic load envelope, with the SOF controller providing a more effective reduction in wing root torsional moments (WRTMs). The load reduction quantification is presented in Table 2.

Table 2. Dynamic load envelope reduction with respect to the baseline aircraft.

Configuration	WRBM	WRTM
SOF	−16.1%	−13.2%
FWT	−14.9%	−1.4%

Both the SOF controller and FWT reduce the wing root bending moment (WRBM) by 15%, while only the SOF controller significantly reduces the wing root torsional moment (WRTM). Physically, FWT reduces the bending moment associated with the outboard wing section, but its impact on the torsional moment is limited, despite the flare angle, creating bending–torsion coupling. In contrast, the aileron deflection generates a counteracting force at the wing tips, associated with a torque caused by the shift of the aerodynamic pressure center in the chord-wise direction. This mechanism enables the SOF controller to effectively reduce the WRTM as well. The optimization of the baseline aircraft ensures that the model is flutter-free across the flight envelope. For the actively controlled aircraft, stability is guaranteed by constraints imposed during SOF tuning, which require the real part of the closed-loop eigenvalues to remain negative. To assess the aeroelastic stability of FWT, a dedicated flutter analysis was performed, and the results, presented as a V-f and V-g plot, are shown in Figure 5.

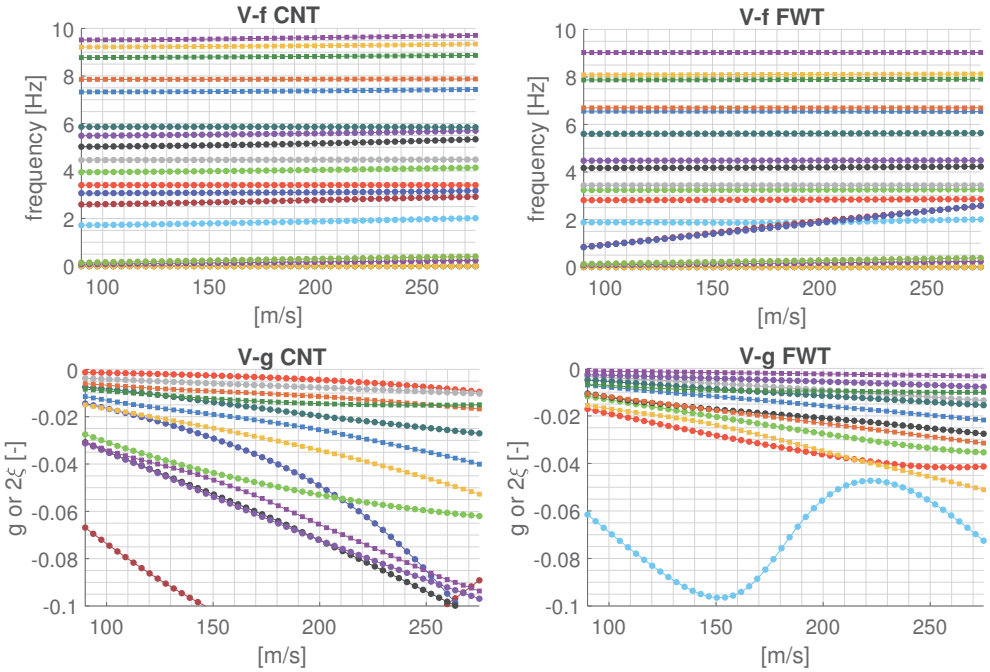

Figure 5. V-g and V-f plots at z = 8000 m.

From the comparison of the V-g diagrams for the CNT and FWT configurations, the FWT solution shows a reduction in the damping of the first wing bending mode between 160 m/s and 220 m/s. However, aeroelastic stability is maintained. To assess the impact on the loads, the transfer function (TF) between the gust input and WRBM was analyzed and compared to that of the CNT aircraft, as shown in Figure 6.

At the frequency corresponding to the first wing bending mode, FWT shows a narrower and higher peak in the transfer function, reflecting the reduced damping observed in the V-g plots. Although FWT's transfer function peak is higher, the dynamic load envelope is still reduced. This is because the input is not a single-tone harmonic but a signal with a broader frequency content. The time response to three gust gradients—namely, the minimum (H = 9 m), the maximum (H = 107 m), and the one tuned to the first wing bending mode (H = 58 m)—is shown in Figure 7, comparing FWT with the CNT configuration. The flight condition is at an altitude of z = 8000 m and a true airspeed of V_{TAS} = 229 m/s,

which corresponds to the point of lowest damping, as indicated in the V-g plot in Figure 5. From now on, this flight condition will be used in all future analyses, as it has proven to be the most critical in terms of internal forces.

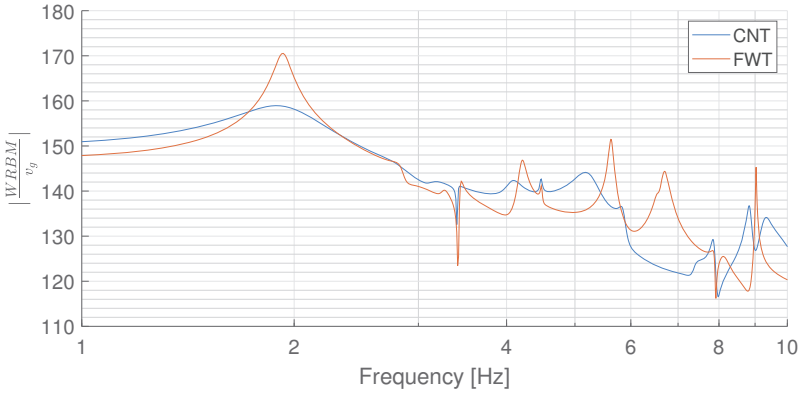

Figure 6. Transfer function between gust velocity and WRBM at z = 8000 m and $V_{TAS} = 229$ m/s.

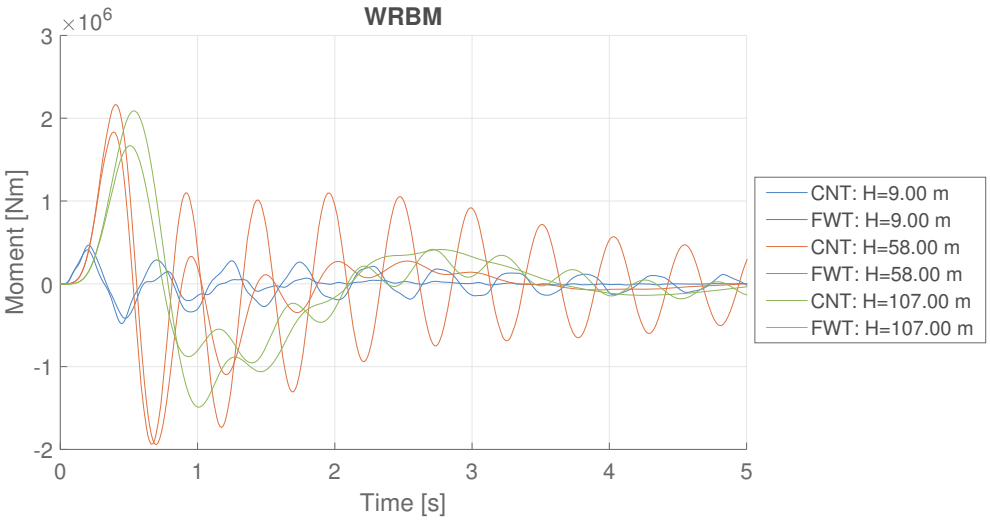

Figure 7. WRBM time response for different gust gradients at z = 8000 m and $V_{TAS} = 229$ m/s.

For all three gust cases considered, the peak WRBM value is reduced with FWT. However, for the tuned gust, there are persistent oscillations over time, which are associated with the reduced damping. This behavior could pose a concern for the fatigue life of the components and must be carefully considered when designing the wing's fatigue durability.

5. Hybrid Model Analysis

To further investigate the behavior of the FWT concept, a detailed model of the wingbox was developed using NeOPT [5]. This model is a fully 3D, high-fidelity finite element (FE) representation of the structural box, where the skins, spar webs, and ribs are modeled with composite shell elements (PCOMP applied to CQUAD4/CTRIA elements). The stringers and spar caps are represented by CBAR elements. The FWT hinge kinematics is modeled similarly to the stick model, with coincident nodes connected by MPCs and a dedicated coordinate system to achieve the desired flare angle. Figure 8 shows the high-fidelity model. The stacking sequence of the composite elements is shown in Figure 9 and the material properties are listed in Table 3.

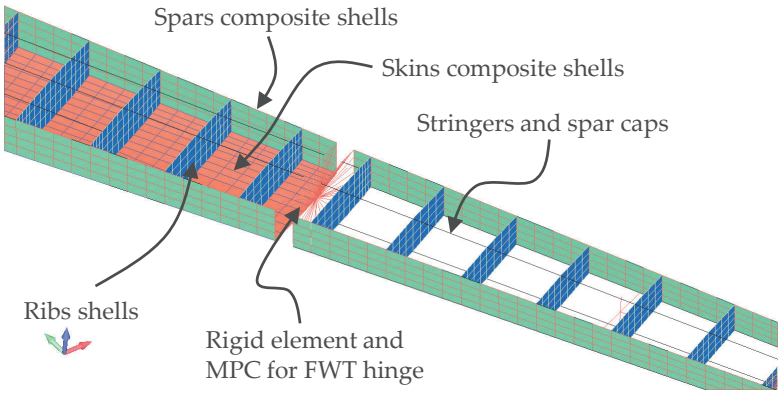

Figure 8. Detailed wingbox close-up with the FWT hinge mechanism highlighted.

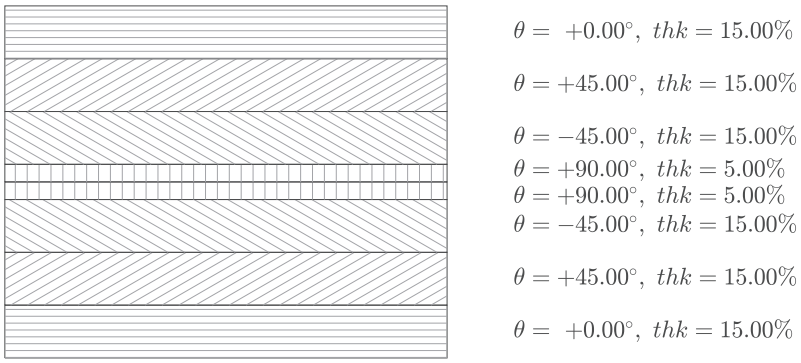

Figure 9. Stacking sequence of composite components, ply thickness is a percentage of the total thickness.

Table 3. Unidirectional carbon fibre structural properties. Full description in the Abbreviation section.

E_{11}	E_{22}	ν_{12}	ν_{21}	G_{12}	G_{13}	G_{23}	ρ	ε_{1T}	ε_{1C}	ε_{2T}	ε_{2C}	γ_{12}
GPa	GPa	-	-	GPa	GPa	GPa	$\frac{kg}{m^3}$	με	με	με	με	με
135	10	0.3	0.022	5	2.8	2.8	1500	5425	2981	3974	12,829	6564

In the dynamic analysis model, the wing structure is replaced with the detailed wingbox, creating a hybrid model for aeroelastic analysis. In this model, the fuselage and tailplanes are represented by a stick skeleton, while the wingbox is fully detailed. The non-structural mass distribution is still modeled using concentrated masses (CONM2). The aerodynamic model remains unchanged as a DLM, with only the splines updated and connected to the rib nodes. The resulting model is shown in Figure 10.

NeoCASS cannot handle shell elements, so the hybrid model was analyzed using Nastran. Due to the significantly higher computational cost compared with the stick model, only three gust conditions were considered. These are the same conditions used to generate the time histories in Figure 7, corresponding to three gust gradients (H = 9, 58, 107 m) at an altitude of 8000 m and $V_{TAS} = 229$ m/s. The validation of the hybrid model is presented in Figures 11–13, where the vertical displacements at the wing root, hinge, and wing tip are compared.

The comparison shows that the response amplitude is the same for both models, although a time shift is observed. This is due to a slightly different natural frequency of the first wing bending mode, which increases from 1.90 Hz in the stick model to 2.03 Hz in the detailed FE model. However, a 6% difference is acceptable, as no updating of the stick model was performed and the connection between the wing and fuselage cannot be modeled in exactly the same way. Additionally, the 3D model has a mass distribution that differs from the stick model, as the stick model is one-dimensional and condenses the 3D properties.

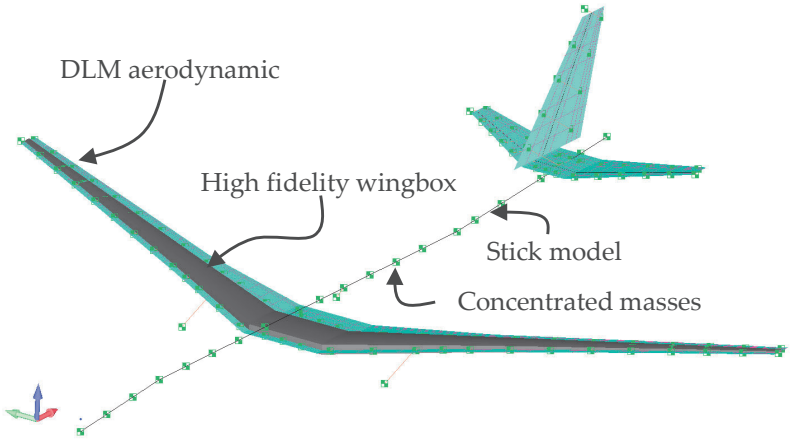

Figure 10. Hybrid aeroelastic model.

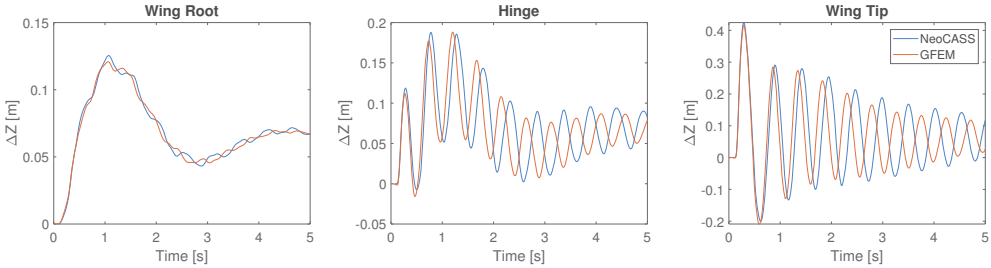

Figure 11. Stick vs. hybrid model vertical displacement comparison. H = 9 m, z = 8000 m, V_{TAS} = 229 m/s.

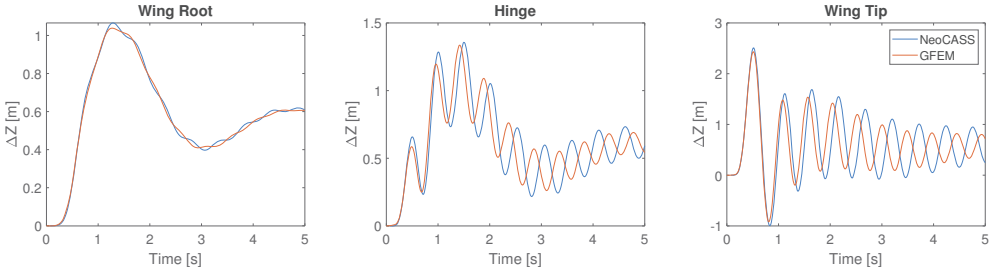

Figure 12. Stick vs. hybrid model vertical displacement comparison. H = 58 m, z = 8000 m, V_{TAS} = 229 m/s.

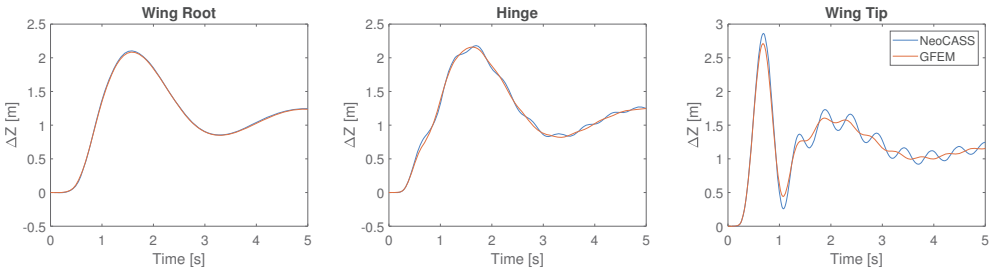

Figure 13. Stick vs. hybrid model vertical displacement comparison. H = 107 m, z = 8000 m, V_{TAS} = 229 m/s.

Overall, the two models show a satisfactory correlation, as their dynamic behavior is similar. With the complete model available, it is possible to investigate detailed structural responses, such as the material's failure indices (FIs), calculated using the maximum strain theory implemented in Nastran's solver. The failure occurs when the FI is larger than 1 (FI > 1). The FIs are monitored on an upper skin element near the wing root, where the bending loads are the highest, but far enough from the carrythrough section to avoid boundary effects. Figure 14 shows the element used to evaluate the FIs. As the laminate is

symmetric and balanced, only the FIs for the first four plies from Figure 9 are presented in Figures 15–17.

The most critical condition occurs with a gust gradient of H = 58 m, particularly for the first ply, which corresponds to the 1st wing bending mode frequency. This condition produces the highest bending moment, as seen in Figure 7, and the same behavior observed for WRBM is present as low-damped oscillations in the FIs, highlighting its potential impact on the fatigue life of the composite skin. For the gust with H = 9 m, the FIs are similar for both models, although this condition is significantly less critical than the H = 58 m gust. In this case, the FIs also exhibit oscillations after the gust hits. A different behavior is observed for the lowest frequency gust with a gradient of H = 107 m. Here, the FI peak is reduced, along with increased damping, resulting in a lower mean FI value for the FWT configuration. Overall, the FIs are lower for the FWT case, which also shows reduced axial stress in the fiber direction for the first ply on both the upper and lower skins. Figures 18 and 19 show a comparison of the fiber direction stress in the first ply of the laminate for the top and bottom skins. The snapshots are taken at the same instant for both the CNT and FWT aircraft.

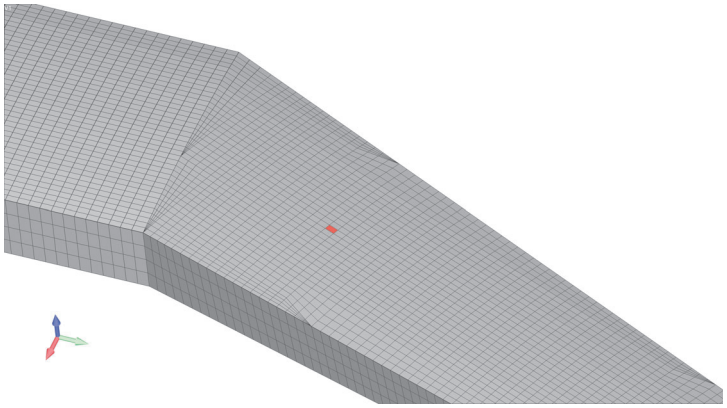

Figure 14. Element used for the FIs evluation.

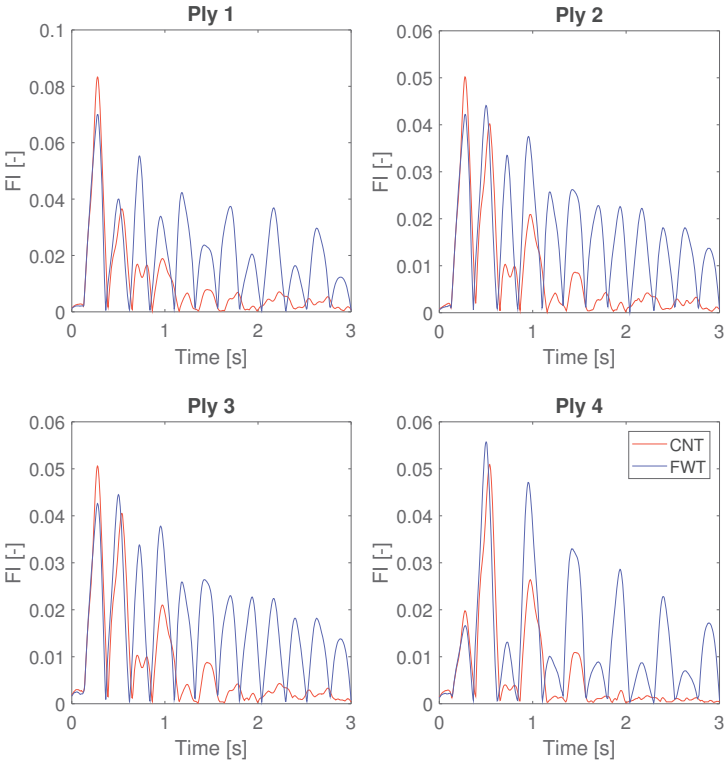

Figure 15. Failure indexes in the laminate. H = 9 m, z = 8000 m, V_{TAS} = 229 m/s.

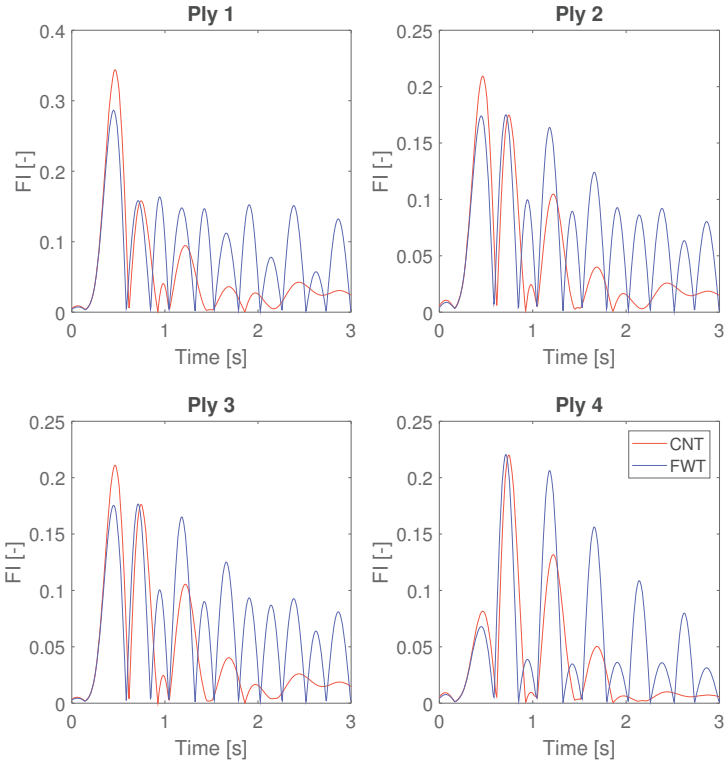

Figure 16. Failure indexes in the laminate. H = 58 m, z = 8000 m, $V_{TAS} = 229$ m/s.

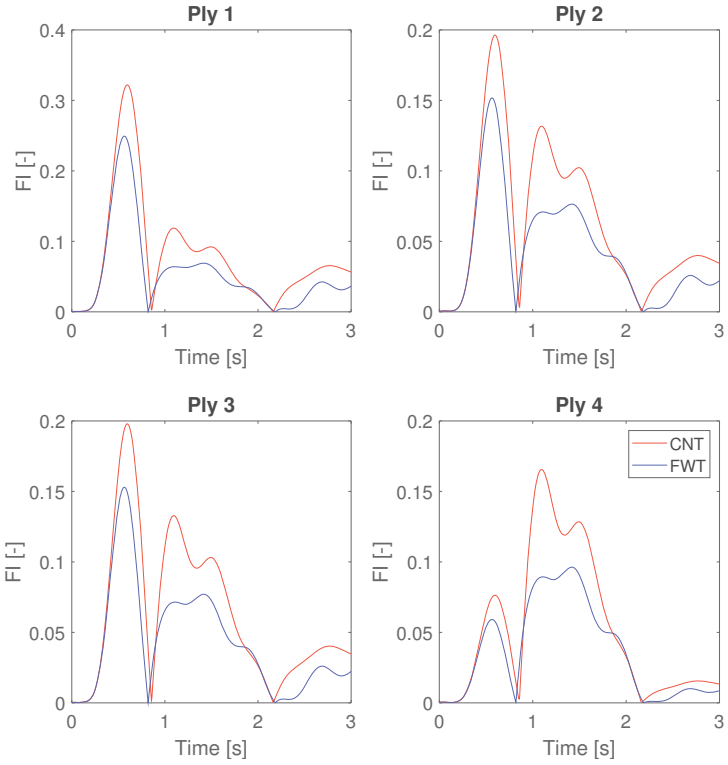

Figure 17. Failure indexes in the laminate. H = 107 m, z = 8000 m, $V_{TAS} = 229$ m/s.

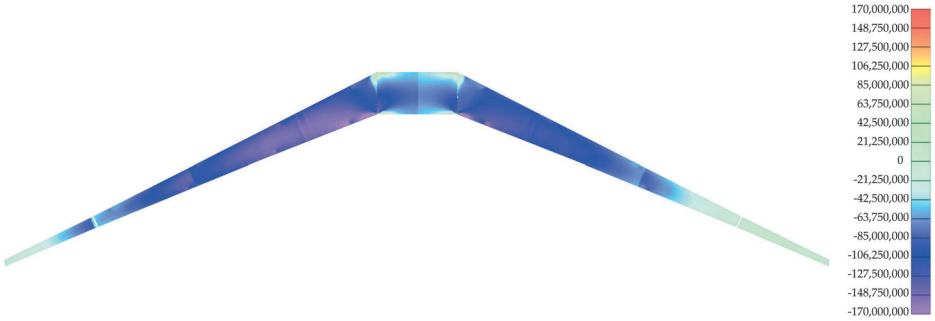

Figure 18. Top skins fibre direction stress in ply 1 comparison between CNT (**left**) and FWT (**right**). t = 0.45 s, H = 58 m, z = 8000 m, $V_{TAS} = 229$ m/s, stress in [Pa].

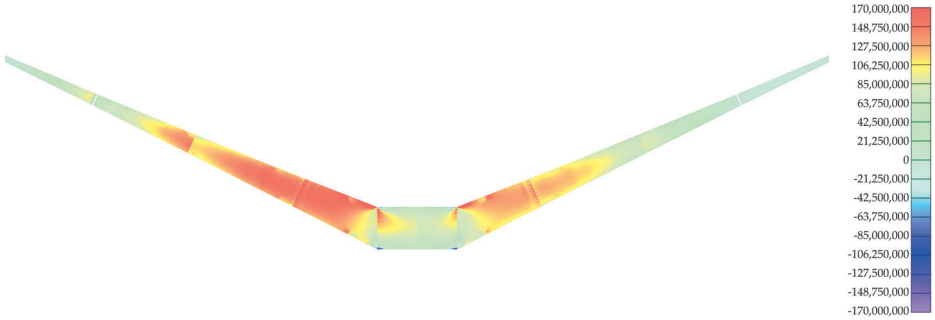

Figure 19. Bottom skins fibre direction stress in ply 1 comparison between CNT (**left**) and FWT (**right**). t = 0.45 s, H = 58 m, z = 8000 m, $V_{TAS} = 229$ m/s, stress in [Pa].

6. Conclusions

This work presents a comparison between two widely studied methods for alleviating dynamic loads caused by gusts. The first method is entirely passive, using a flared folding wing tip (FWT), while the second involves an active controller based on a static output feedback (SOF) scheme. Both approaches effectively reduce the wing root bending moment (WRBM) of about 15%, with the SOF also reducing the wing root torsional moment (WRTM) of 13%. However, a drawback of FWT is its reduced damping within the flight envelope, which, while maintaining aircraft stability, could pose greater challenges for fatigue. An advanced hybrid finite element (FE) aeroelastic model, in which the wing was replaced by a detailed 3D wingbox, was used to analyze the structural response in terms of failure indices (FIs). The FIs were found to be lower for the FWT configuration (-17%), but the reduced aeroelastic damping led to a low-damped oscillatory response. This issue must be addressed from the early design phases, considering both fatigue life and load reduction.

Although the two load alleviation systems provide nearly the same load reduction for the wing root bending moment (WRBM), other factors must be considered. The impact on fatigue has already been highlighted, and it could be mitigated by incorporating a damper in the folding wing tip (FWT) hinge. While it is true that FWT allows for an increased wingspan without requiring changes to the aircraft's aerodrome reference code (ARC), it also necessitates a dedicated system for sensing, actuation, and folding the wing, as well as releasing it during gusts and restoring its flight shape afterward. On the other hand, active gust load alleviation (GLA) can use conventional wing architecture and sensors to achieve a similar load reduction. However, the wingspan increase is constrained by the aircraft's ARC, and modifying this for ground operations is not as straightforward. All these aspects must be carefully considered during the conceptual design phase to determine the most cost-effective and practical solution.

Funding: This research was funded by Grant Agreement number: 886552-H2020-CS2-CFP10-2019-01.

Institutional Review Board Statement: Not applicable.

Informed Consent Statement: Not applicable.

Data Availability Statement: The data presented in this study are available upon request from the corresponding author.

Acknowledgments: The support of J. E. Cooper and H. Gu from University of Bristol is highly appreciated. The U-HARWARD Project has received funding from the Clean Sky 2 Joint Undertaking, under the European's Union Horizon 2020 research and innovation Program under Grant Agreement number: 886552-H2020-CS2-CFP10-2019-01. The content of this document reflects only the author's view. The European Commission and Clean Sky 2 Joint Undertaking (CS2JU) are not responsible for any use that may be made of the information it contains.

Conflicts of Interest: The author declare no conflicts of interest.

Abbreviations

The following abbreviations are used in this manuscript:

$\nu_{\bullet\circ}$	Poisson's ration in $\bullet\circ$ directions
ρ	Density
$\gamma_{\bullet\circ}$	Allowable strain for $\bullet\circ$ direction shear
$\varepsilon_{\bullet T}$	Allowable strain in $\bullet$ direction in tension
$\varepsilon_{\bullet C}$	Allowable strain in $\bullet$ direction in compression
$E_{\bullet}$	Elastic modulus in $\bullet$ direction
$G_{\bullet\circ}$	Transverse shear modulus in $\bullet\circ$ directions
ARC	Aerodrome Reference Code
BM	Bending Moment
CG	Center of Gravity
CL	Closed Loop
CNT	Cantilevered
DLM	Doublette Lattice Method
EAS	Equivalent Air Speed
ES	Engine Section
FE(M)	Finite Element (Method)
FI	Failure Index
FWT	Folding Wing Tip
GAFs	Generalized Aerodynamic Forces
GFEM	Global Finite Element Model
GLA	Gust Load Alleviation
LH	Left Hand
MFA	Matrix Fraction Approximation
MPC	Multiple Point Constraint
OL	Open Loop
RH	Right Hand
SOF	Static Output Feedback
TAS	True Air Speed
TF	Transfer Function
TM	Torsional Moment
WR	Wing Root

References

1. Carrier, G.; Arnoult, G.; Fabbiane, N.; Schotté, J.S.; David, C.; Defoort, S.; Delavenne, M.; Bénard, E. Multidisciplinary Analysis and Design of Strut-Braced Wing Concept for Medium Range Aircraft. In Proceedings of the AIAA Science and Technology Forum and Exposition, AIAA SciTech Forum 2022, San Diego, CA, USA, 3–7 January 2022. [CrossRef]
2. Ricci, S.; Paletta, N.; Defoort, S.; Benard, E.; Cooper, J.E.; Barabinot, P. U-HARWARD: A CS2 EU Funded Project Aiming at the Design of Ultra High Aspect Ratio Wings Aircraft. In Proceedings of the AIAA Science and Technology Forum and Exposition, AIAA SciTech Forum 2022, San Diego, CA, USA, 3–7 January 2022. [CrossRef]
3. Marchetti, L.; Toffol, F.; Ricci, S.; Beretta, J.; Paletta, N. Aeroelastic Optimization of High Aspect Ratio Wings for Environmentally Friendly Aircraft. In Proceedings of the AIAA Science and Technology Forum and Exposition, AIAA SciTech Forum 2022, San Diego, CA, USA, 3–7 January 2022. [CrossRef]

4. Toffol, F.; Ricci, S. Preliminary Aero-Elastic Optimization of a Twin-Aisle Long-Haul Aircraft with Increased Aspect Ratio. *Aerospace* **2023**, *10*, 374. [CrossRef]
5. Toffol, F.; Ricci, S. A Meta-Model for Composite Wingbox Sizing in Aircraft Conceptual Design. *Compos. Struct.* **2023**, *306*, 116557. [CrossRef]
6. Tang, D.; Dowell, E.H. Experimental and Theoretical Study of Gust Response for High-Aspect-Ratio Wing. *AIAA J.* **2002**, *40*, 419–429. [CrossRef]
7. Sanghi, D.; Cesnik, C.E.; Riso, C. Roll Maneuverability of Transonic High-Aspect-Ratio-Wing Aircraft with Flared Folding Wingtips. *J. Aircr.* **2024**, *61*, 915–938. [CrossRef]
8. Afonso, F.; Vale, J.; Oliveira, É.; Lau, F.; Suleman, A. A Review on Non-Linear Aeroelasticity of High Aspect-Ratio Wings. *Prog. Aerosp. Sci.* **2017**, *89*, 40–57. [CrossRef]
9. Abouhamzeh, M.; Ma, Y.; Elham, A. A Geometrically Nonlinear Structural Model for Aerostructural Optimization of Ultra-High Aspect Ratio Composite Wings. In Proceedings of the AIAA Science and Technology Forum and Exposition, AIAA SciTech Forum 2022, San Diego, CA, USA, 3–7 January 2022. [CrossRef]
10. Marchetti, L.; Ricci, S.; Riccobene, L.; Grassi, D.; Mantegazza, P.; Adden, S.; Gu, H.; Cooper, J. Gust Load Alleviation Wind Tunnel Tests of a Folding Wing Tip Configuration. In Proceedings of the International Forum of Aeroelasticity and Structural Dynamics 2024, IFASD 2024, The Hague, The Netherlands, 17–21 June 2024.
11. Barnes, C.H.; Derek, J. *Shorts Aircraft Since 1900*; Putnam Aeronautical Books, an imprint of Conway Maritime Press; Conway Maritime Press: London, UK, 1989.
12. Tillman, B. Does the Douglas TBD-1 Devastator Deserve Its Bad Rap? 2022. Available online: https://www.historynet.com/does-the-douglas-tbd-1-devastator-deserve-its-bad-rap/ (accessed on 22 October 2024).
13. Pace, S. *North American XB-70 Valkyrie*; TAB Books: New York, NY, USA, 1990.
14. Lassen, M.A.; Douglas, C.R.; Jones, K.T.; Kenning, T.B. Wing Fold Controller Patent. Patent Number: EP 2 727 829 B1, 5 September 2018. Available online: https://patentimages.storage.googleapis.com/1a/11/a1/9e515a7fc9a06d/EP2727829B1.pdf (accessed on 22 October 2024).
15. Anonymous. Knee Action Wings Cushion Ride In French Plane. *Pop. Sci.* **1951**, *158*, 150–151.
16. Pitt, D.M. Static and Dynamic Aeroelastic Analysis of Structural Wing Fold Hinges That are Employed as an Aeroelastic Tailoring Tool. In Proceedings of the Collection of Technical Papers—AIAA/ASME/ASCE/AHS/ASC Structures, Structural Dynamics and Materials Conference, Palm Springs, CA, USA, 19–22 April 2004; Volume 4. [CrossRef]
17. Wilson, T.; Castrichini, A.; Azabal, A.; Cooper, J.; Ajaj, R.; Herring, M. Aeroelastic Behaviour of Hinged Wing Tips. In Proceedings of the International Forum of Aeroelasticity and Structural Dynamics 2015, IFASD 2015, St. Petersburg, Russia, 28 June–2 July 2015.
18. Siddaramaiah, V.H.; Calderon, D.E. *Preliminary Studies in the Use of Folding Wing—Tips for Loads Alleviation*; Royal Aeronautical Society: Bristol, UK, 2014.
19. Ye, B.; Yang, Y.; Cheng, Z. Flare folding wing tips for static and gust loads alleviation. *J. Phys. Conf. Ser.* **2023**, *2459*, 012071. [CrossRef]
20. Ajaj, R.M.; Saavedra Flores, E.I.; Amoozgar, M.; Cooper, J.E. A parametric study on the aeroelasticity of flared hinge folding wingtips. *Aerospace* **2021**, *8*, 221. [CrossRef]
21. Castrichini, A.; Saltari, F.; Viceconti, N.; Wilson, T.; Cooper, J.E.; Mastroddi, F. Aeroelastics flight dynamics coupling effects of the semi aeroelastic hinge device—IFASD 2019. In Proceedings of the International Forum on Aeroelasticity and Structural Dynamics 2019, IFASD 2019, Savannah, GA, USA, 9–13 June 2019.
22. Castrichini, A.; Hodigere Siddaramaiah, V.; Calderon, D.E.; Cooper, J.E.; Wilson, T.; Lemmens, Y. Nonlinear folding wing tips for gust loads alleviation. *J. Aircr.* **2016**, *53*, 1391–1399. [CrossRef]
23. Castrichini, A.; Cooper, J.E.; Wilson, T.; Carrella, A.; Lemmens, Y. Nonlinear Negative Stiffness Wingtip Spring Device for Gust Loads Alleviation. *J. Aircr.* **2017**, *54*, 627–641. [CrossRef]
24. Castrichini, A.; Siddaramaiah, V.H.; Calderon, D.E.; Cooper, J.E.; Wilson, T.; Lemmens, Y. Preliminary Investigation of Use of Flexible Folding Wing Tips for Static and Dynamic load Alleviation. *Aeronaut. J.* **2017**, *121*, 73–94. [CrossRef]
25. Hayes, D.; Lone, M.; Whidborne, J.F.; Coetzee, E. Evaluating the rationale for folding wing tips comparing the exergy and breguet approaches. In Proceedings of the AIAA SciTech Forum—55th AIAA Aerospace Sciences Meeting, Grapevine, TX, USA, 9–13 January 2017. [CrossRef]
26. Wilson, T.; Kirk, J.; Hobday, J.; Castrichini, A. Small scale flying demonstration of semi aeroelastic hinged wing tips. In Proceedings of the International Forum on Aeroelasticity and Structural Dynamics 2019, IFASD 2019, Savannah, GA, USA, 9–13 June 2019.
27. Cheung, R.C.; Castrichini, A.; Rezgui, D.; Cooper, J.E.; Wilson, T. Testing of wing-tip spring device for gust loads alleviation. In Proceedings of the 58th AIAA/ASCE/AHS/ASC Structures, Structural Dynamics, and Materials Conference, Grapevine, TX, USA, 9–13 January 2017. [CrossRef]
28. Cheung, R.C.; Rezgui, D.; Cooper, J.E.; Wilson, T. Testing of folding wing-tip for gust load alleviation in high aspect ratio wing. In Proceedings of the AIAA Scitech 2019 Forum, San Diego, CA, USA, 7–11 January 2019. [CrossRef]
29. Harpur, N.F. The Effect of Active Control System on Structural Design Criteria. In *Active Control Systems for Load Alleviation, Flutter Suppression and Ride Control*; AGARD: Paris, France, 1974; pp. 11–22.

30. Regan, C.D.; Jutte, C.V. *Survey of Applications of Active Control Technology for Gust Alleviation and New Challenges for Lighter-Weight Aircraft*; NASA/TM—2012–216008; NASA: Washington, DC, USA, 2012.
31. Cooper, J.E.; Gu, H.; Ricci, S.; Toffol, F.; Adden, S.; Meheut, M.; Benard, E.; Barabinot, P. CS2-THT U-HARWARD Project: Final Assessment and Project Outcomes Evaluation. In Proceedings of the AIAA SciTech Forum and Exposition 2024, Orlando, FL, USA, 8–12 January 2024. [CrossRef]
32. Toffol, F. Passive and Active Load Alleviation Technologies for UHARW Wings. In Proceedings of the International Forum of Aeroelasticity and Structural Dynamics 2024, IFASD 2024, The Hague, The Netherlands, 17–21 June 2024.
33. Fonte, F.; Ricci, S.; Mantegazza, P. Gust Load Alleviation for a Regional Aircraft Through a Static Output Feedback. *J. Aircr.* **2015**, *52*, 1559–1574. [CrossRef]
34. Toffol, F.; Marchetti, L.; Ricci, S.; Fonte, F.; Capello, E.; Malisani, S. Gust and Manouvre Loads Alleviation Technologies: Overview, Results and Lesson Learned in the Framework of the CS2 AIRGREEN2 Project. In Proceedings of the International Forum of Aeroelasticity and Structural Dynamics 2022, IFASD 2022, Madrid, Spain, 13–17 June 2022.
35. Healy, F.; Gu, H.; Rezgui, D.; Cooper, J. Nonlinear Stability Analysis of Floating Wingtips with Control Surface Freeplay. In Proceedings of the AIAA SciTech Forum and Exposition 2024, Orlando, FL, USA, 8–12 January 2024. [CrossRef]
36. Gu, H.; Healy, F.; Jayatilake, S.; Rezgui, D.; Lowenberg, M.; Cooper, J.; Wilson, T.; Castrichini, A. Flight Dynamics of Aircraft Incorporating the Semi-Aeroelastic Hinge. *Aerosp. Sci. Technol.* **2024**, *147*, 109026. [CrossRef]
37. Gu, H.; Healy, F.; Rezgui, D.; Cooper, J. Sizing of High-Aspect-Ratio Wings with Folding Wingtips. *J. Aircr.* **2023**, *60*, 461–475. [CrossRef]
38. Ripepi, M.; Mantegazza, P. Improved Matrix Fraction Approximation of Aerodynamic Transfer Matrices. *AIAA J.* **2013**, *51*, 1156–1173. [CrossRef]
39. EASA. Certification Specifications for Large Aeroplanes CS25. 2024. Available online: https://www.easa.europa.eu/en/document-library/certification-specifications/group/cs-25-large-aeroplanes (accessed on 22 October 2024).
40. Syrmos, V.L.; Abdallah, C.T.; Dorato, P.; Grigoriadis, K. Static output feedback—A survey. *Automatica* **1997**, *33*, 125–137. [CrossRef]
41. Toffol, F. Aero-Servo-Elastic Optimization in Conceptual and Preliminary Design. Ph.D. Thesis, Politecnico di Milano, Milano, Italy, 2021.
42. Ricci, S.; Toffol, F.; De Gaspari, A.; Marchetti, L.; Fonte, F.; Riccobene, L.; Mantegazza, P.; Berg, J.; Livne, E.; Morgansen, K. Wind Tunnel System for Active Flutter Suppression Research: Overview and Insights. *AIAA J.* **2022**, *60*, 6692–6714. [CrossRef]